




Microstructure and mechanical properties of Tribaloy coatings deposited by high-velocity oxygen fuel

S. A. Alidokht¹, Y. Gao¹, B. C. N. M. de Castilho¹, N. Sharifi², M. Harfouche¹,
P. Stoyanov³, M. Makowiec⁴, C. Moreau², and R. R. Chromik^{1,*} 

¹Department of Mining and Materials Engineering, McGill University, M. H. Wong Building, 3610 University Street, Montreal, QC H3A 0C5, Canada

²Mechanical, Industrial and Aerospace Engineering, Concordia University, EV Building, 1515 St. Catherine W., Montreal, QC H3G 2W1, Canada

³Chemical and Materials Engineering, Concordia University, 1455 De Maisonneuve Blvd. W., Montreal, QC H3G 1M8, Canada

⁴Pratt & Whitney, 400 Main Street, East Hartford, CT 06118, USA

Received: 16 June 2022

Accepted: 8 October 2022

Published online:
22 October 2022

© The Author(s), under
exclusive licence to Springer
Science+Business Media, LLC,
part of Springer Nature 2022

ABSTRACT

Triballoys are Cobalt-based alloys with general composition M–Mo–Cr–Si (M = Co), with a microstructure of Laves intermetallic phases dispersed in a Co solid solution. The chemical composition plays a major role in volume fractions of the strengthening phases in these alloys, which in turn dictate the mechanical properties and tribological performance of these materials. In this study, two Co-based Triballoy powders, i.e., Co-28.5Mo-17.5Cr-3.4Si and Co-28.5Mo-8.5Cr-2.6Si, were coated on mild steel substrate by high-velocity oxygen fuel (HVOF) spraying. Microstructure and distribution of Laves phases were studied using scanning electron microscopy (SEM) equipped with energy-dispersive X-ray (EDX) analysis as well as electron channeling contrast imaging (ECCI). Detailed phase analysis of powders and coatings was performed using X-ray diffraction (XRD). Electron backscatter diffraction (EBSD) was conducted on sprayed coatings to reveal the distribution of phases in coatings. Co₃Mo₂Si and Co₃Mo were found to be the main constituent of intermetallic Laves phases in HVOF-sprayed coatings. A significantly lower volume fraction of Laves phases was identified in both coatings as compared to similar alloys in the literature, due to an extremely high cooling rate and solidification in HVOF. The Laves-free solid solution featured nano-crystalline microstructure with a similar local hardness to those of Laves phases. Highly flattened splats that contained nano-crystalline supersaturated solid solution displayed weak interfaces within the microstructure where cracks initiated and propagated along boundaries during splat cohesion testing.

Handling Editor: Maude Jimenez.

S. A. Alidokht and Y. Gao contributed equally to this work.

Address correspondence to E-mail: richard.chromik@mcgill.ca

Introduction

High-Velocity Oxy-Fuel (HVOF) thermal spraying produces relatively dense metallic and composite coatings for a wide range of applications [1]. One example of the commercial coatings system developed by thermal spray techniques is Co-based Triballoys. The CoMoCrSi alloys, mostly known as Tribaloy® family, display outstanding wear-resistant and corrosion-resistant properties for applications in which extreme wear is combined with high temperatures and corrosive media, such as industrial turbine applications [2–6]. The most frequently used Cobalt-based Tribaloy alloys are T400, T-800, and T-900. These alloys are usually hypereutectic alloys that feature 35–70% hard intermetallic Laves phases which are dispersed in a tough matrix of eutectic or solid solution. The hard Laves phase crystal structures are MgZn₂-type with a melting point of about 1560 °C. Previous studies have found that the mechanical properties and wear performance of these alloys depend highly on the volume fraction of the Laves phase [2–7].

Microstructure and characteristics of welded or laser clad Triballoys are well documented in previous studies. Dense and pore-free layers were reported to be deposited using laser cladding with a relatively high adherence following a metallurgical bonding with the substrate [5–9]. Owing to peculiarities of thermal spraying processes, the microstructure, and properties of thermal sprayed Triballoys are significantly different than those for laser cladding. A fully crystalline microstructure is identified in laser clad or welded triballoy, whereas for thermal sprayed Tribaloy, the coatings are built upon high-velocity impact of heated particles which creates a lamellar microstructure. Besides, splats quench upon impact at a very high cooling rate (about 10⁵ K/s) which results in the formation of metastable phases, supersaturated solid solution, and a very fine microstructure sometimes nano-crystalline or even amorphous phases within splats [4, 10]. Therefore, the knowledge that is provided by studies on welded or laser clad Tribaloy cannot directly be applied to thermal spray and in particular HVOF coatings. More studies are needed to further characterize the mechanical behavior of such coatings when produced by HVOF, especially when considering the requirements of the aerospace industry. This research therefore aims to

provide a detailed characterization of Diamalloy 3001 (similar to Tribaloy 800) and Diamalloy 3002NS (similar to Tribaloy 400). This includes microstructural and phase analysis of feedstock powders and coatings, as well as mechanical properties evaluation of individual phases. In addition, scratch testing was performed on the cross section of coatings to evaluate the inter-splat cohesion.

Experimental

Two commercially available thermal spray powders, i.e., Diamalloy 3001 (Sulzer Metco, Oerlikon Metco, Canada) and Diamalloy 3002NS (Sulzer Metco, Oerlikon Metco, Canada) were used as feedstock materials. Diamalloy 3001 and 3002NS are trade names of specific Tribaloy materials made by Oerlikon Metco. The chemical composition of Diamalloy 3001 and Diamalloy 3002NS powders (Table 1) was similar to that of Tribaloy 800 and Tribaloy 400, respectively, where Diamalloy 3001 has higher percentages of Cr and Si. Diamalloy 3002NS powder was water atomized, whereas gas atomization was the manufacturing route for Diamalloy 3001 powder. Laser particle size analysis (LA-920, Horiba, Japan) was used to measure feedstock powder size distribution.

The coatings were sprayed by HVOF using a Diamond Jet 2700 gun (Sulzer Metco, USA), and propylene was used as fuel. A preliminary set of tests was carried out by varying the oxygen-to-fuel (O/F) ratio and measuring the deposition efficiency of the process. The spray condition with the highest deposition efficiency (about 55%) was selected to produce the coatings. The selected deposition conditions are presented in Table 2. The flow rate of 70 and 303 l/min for fuel and oxygen, respectively, provides an oxygen-to-fuel ratio of approximately 5.38 and yielding a mixture with approximately 20% of oxygen in excess during the combustion. Particle temperature for both powders was, on average, between 2000 and 2200 °C,

Table 1 Chemical Composition of Diamalloy 3001 and Diamalloy 3002NS feedstock powders

Feedstock	Co	Mo	Cr	Si
Nominal Composition wt.%				
Diamalloy 3001	Balance	28.5	17.5	3.4
Diamalloy 3002NS	Balance	28.5	8.5	2.6

which is above the melting point of the powders. The particle velocity was also similar for both powders, between 550 and 570 m/s. The temperature of the mild steel substrate reached no more than 300 °C during spraying.

X-ray diffraction (Discover D8 diffractometer, Bruker, USA) of feedstock powders and HVOF-sprayed coatings was done with 2D HISTAR area detector, source of Co K α radiation (1.79 Å) at 35 kV and 45 mA and then indexed from ICDD JCPDS Standards. The samples for XRD were the same as those prepared for scanning electron microscopy (SEM) studies. HVOF-sprayed coatings were cross-sectioned using an abrasive cutter and then cold mounted in epoxy, containing a conductive copper filler. Mounted samples were mechanically ground using 240, 320, 400, 600, 800, and 1200 grit grinding papers, followed by polishing using 9, 3, and 1 μ m diamond suspension. The samples were vibratory polished using 0.05 μ m colloidal silica for 3 h to remove residual stress induced by cutting, grinding, and polishing steps. Similar procedures of grinding and polishing were used for mounted feedstock powder but subjected to vibratory polishing for 12 h.

The morphology of the initial powders was observed by SEM (SU3500, Hitachi, Japan) equipped with Oxford AZtec X-Max50 SDD energy-dispersive detector (EDS). Electron channeling contrast imaging (ECCI) using a cold field emission SEM (SU-8230, Hitachi, Japan), with a photodiode backscattered electron (BSE) detector, was used to reveal the microstructure of the initial powders and deposited coatings. An Ar + ion milling system (IM3000 flat) was used to remove the top surface that might contain polishing-induced deformation. An open-source software, ImageJ, was used to analyze the area fraction of pores, Laves regions (primary Laves and

eutectic), and Laves-free solid solution in HVOF-sprayed coatings.

The electron backscatter diffraction (EBSD) was performed with SEM (SU3500, Hitachi, Japan) equipped with EBSD (Oxford Instruments 2014) to identify phases in HVOF-sprayed coatings. The step size ranged between 100 and 200 nm, and a 70° tilt was used. Tango software (HKL CHANNEL 5, Oxford) was used to analyze and output EBSD data, including band contrast image, phase image, and mean angular distribution (MAD) image. MAD, which is the angular deviation between the observed and simulated lattice plane orientations [11–13], has been used to determine the goodness of fit. The smaller the value of MAD, the better the match between the detected Kikuchi bands and the simulation. MAD values of under 1° are considered as indicators of an acceptable fit.

Nano-indentation mapping was performed on the polished cross section of coatings to investigate the mechanical properties of phases. Nano-indentation measurements were carried out at room temperature using Triboindenter system (TI 950, Hysitron, USA). A diamond indenter of Berkovich geometry was used. For all the indentations, a scheme of 5–2–5, i.e., 5 s loading, 2 s holding at peak load, and 5 s of unloading time was used. The load–displacement curve was obtained and then analyzed using Oliver–Pharr method [14] to calculate the hardness and reduced modulus described as follows. The stiffness (S) of a material, which was measured as the slope at the onset of unloading curve ($\frac{dp}{dh}$), and the projected contact area (A) were used to calculate the reduced modulus using the following equations [14]:

$$S = \frac{dp}{dh} = \frac{2}{\sqrt{\pi}} E_r \sqrt{A} \quad (1)$$

$$\frac{1}{E_r} = \left(\frac{1 - \nu^2}{E} \right)_{\text{specimen}} + \left(\frac{1 - \nu^2}{E} \right)_{\text{indenter}} \quad (2)$$

where E_r is the reduced modulus calculated from the elastic moduli of the indenter and tested specimen and their Poisson ratios, ν . The projected area A is dependent on the contact depth h_c of the indenter according to the indenter area function, for Berkovich indenter [15, 16].

The hardness of the coating is measured by the following equation [15, 16]:

Table 2 HVOF deposition conditions

Parameter	Value
Propylene flow rate (l/min)	79
Oxygen flow rate (l/min)	303
Air flow rate (l/min)	422
Carrier gas	Nitrogen
Feedstock flow rate (g/min)	23
Stand-off distance (mm)	150
Robot speed (mm/s)	1000
Number of passes	10

$$H = \frac{P_{\max}}{A} \quad (3)$$

After nano-indentation testing, SEM imaging was performed to locate the indents on individual phases. To identify mechanical properties of phases that are present in coatings, indent arrays were superimposed with EBSD phase images.

Scratch testing (Micro-Combi, Anton Paar, Switzerland) was performed on coatings cross sections according to the ISO/WD27307 working draft [17, 18] to characterize the cohesive bond strength of the coatings. A Diamond Rockwell indenter with a radius of 20 μm was used. Constant normal loads of 0.25, 1, 2, 3, 4, and 5 N were tested. Scratch speed was kept constants for all tests at 3.5 mm/min to keep results consistent and comparable among each other. The scratch length was kept at 1.4 mm for all tests and started in the substrate and finished in the resin. The scratch tracks were observed by an SEM to reveal the failure mechanism and splat de-cohesion. A qualitative comparison of the cohesive strength of the coatings was developed.

Results and discussion

Powders characterization

Figure 1 shows the morphology of feedstock powders. Diamalloy 3001 powders exhibited spherical morphology, whereas an irregular morphology was identified for Diamalloy 3002NS. The particle size distribution was measured by laser diffraction size analysis (Fig. 2). Diamalloy 3001 and 3002NS powders had particle size range of $-36 + 15 \mu\text{m}$ ($d_{50} = 25 \mu\text{m}$) and $-68 + 22 \mu\text{m}$ ($d_{50} = 42 \mu\text{m}$), respectively. Particle morphology was consistent with the method of manufacture, where Diamalloy 3001 was gas atomized and Diamalloy 3002 was water atomized.

XRD phase analysis was performed on powder particles and the diffractograms are given in Fig. 3a and b for 3001 and 3002NS powders, respectively. Both as-received Diamalloy powders registered a crystalline structure and consisted mainly of Co–Cr–Mo and Cr–Co–Si solid solutions, as well as Co–Mo Laves intermetallic phases of Co_7Mo_6 and Co_3Mo . Crystal structures in cobalt alloys, including Co-based solid solutions, can be either face-centered cubic or hexagonal, whereas Cr–Co–Si solid solution

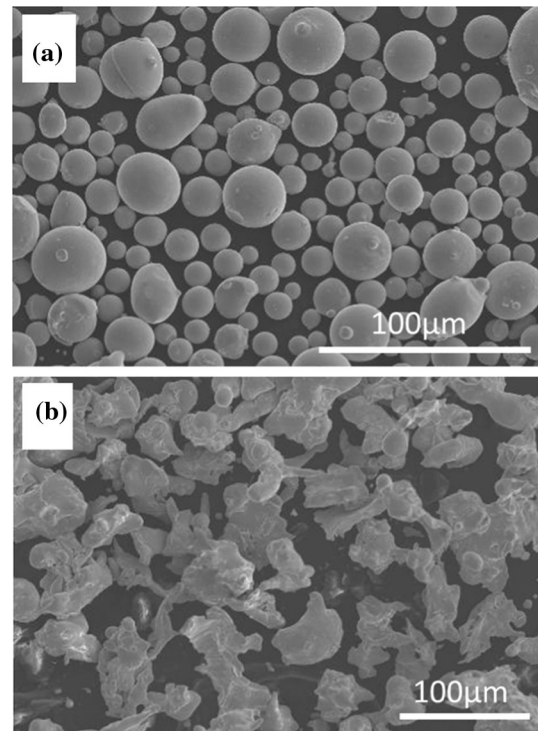


Figure 1 Morphology of as-received powders: **a** Diamalloy 3001 and **b** Diamalloy 3002NS powders.

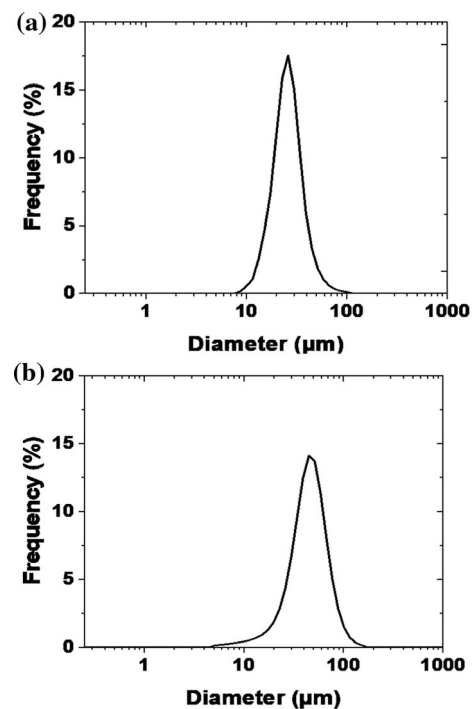


Figure 2 Size distribution of the as-received powders: **a** Diamalloy 3001 and **b** Diamalloy 3002NS powders.

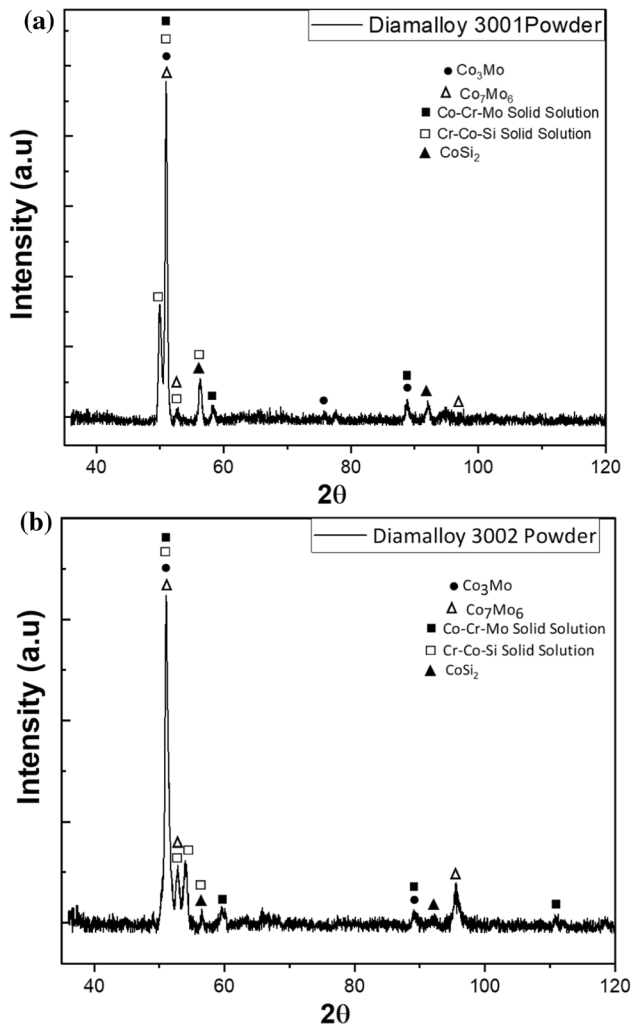


Figure 3 XRD phase characterization of **a** Diamalloy 3001 and **b** 3002NS powders.

is in tetragonal structure. Co_7Mo_6 Lave phase is in hexagonal and Co_3Mo in cubic structures [19–21].

The microstructure of the as-received Diamalloy 3001 and 3002NS powders is given in Figs. 4 and 5, respectively. The primary Laves phase of star or butterfly morphology for both powder particles can be observed. Besides the primary Laves phase, a eutectic aggregate, as well as Laves-free solid solutions phases, is identified. Eutectic aggregates consisted of solid solution and secondary Laves lamellas. Comparing the microstructure of Diamalloy 3001 and 3002NS powders, the latter exhibits a finer composite microstructure consisted of fine lamellar Laves phases in solid solution. This could be partly due to the higher cooling rate in water atomization compared to gas atomization, which was the processing route for Diamalloy 3001 powder. This observation is also

consistent with the previous studies where the same manufacturing methods have been used for similar alloys [19, 21].

Chemical analysis of various microstructures is performed and shown in Figs. 4c–d and 5c–d for Diamalloy 3001 and 3002NS, respectively. Laves phases for both powders are composed of higher Mo and Si and lower Cr and Co as compared to that of the nominal composition of the powders. Laves-free solid solutions were of similar elemental composition as the nominal composition of powders, whereas solid solutions in eutectic aggregates were rich in Cr but contain a lower amount of Mo.

Coatings characterization

Microstructure

Figures 6 and 7 show micrographs of Diamalloy 3001 and 3002NS coatings. Coatings' thicknesses were 98 ± 6 and 86 ± 7 μm for Diamalloy 3001 and 3002NS, respectively. Lamellar structure typical to thermal sprayed coatings can be seen for both coatings. Both Diamalloy 3001 and 3002NS coatings consist of flattened splats, rounded unmelted or partially melted particles as well as pores and intersplat gaps/cracks. Micrographs collected from coatings show Laves phases only retained in some of the rounded particles, whereas highly flattened splats are Laves-free regions. Higher magnification images from regions containing Laves phases show various microstructural features. This includes coarse primary Laves of star or butterfly dendritic morphology that are preserved from rapid solidification as well as eutectic phase consisted of Laves dendrites and dark-contrast solid solutions. The area fraction of various microstructural features for both coatings is measured and reported in Table 3. For Diamalloy 3002NS, the area fraction of pores was significantly lower than that for Diamalloy 3001 coatings. Previous studies have reported 40–70 vol.% for area fraction of Laves regions in as-cast trialloys, with Tribaloy 800 containing a higher fraction of Laves phases [2–7]. Here, for Diamalloy 3001, similar composition to Tribaloy 800, this was found to be 36 ± 4 vol.%, close to the lower end of the range reported in the literature [2–7], whereas, for Diamalloy 3002NS coatings, this was 28 ± 4 vol.%. This is due to an extremely high cooling rate ($> 10^5$ K/s) that particles are exposed to upon impact in HVOF, causing splat quenching. This

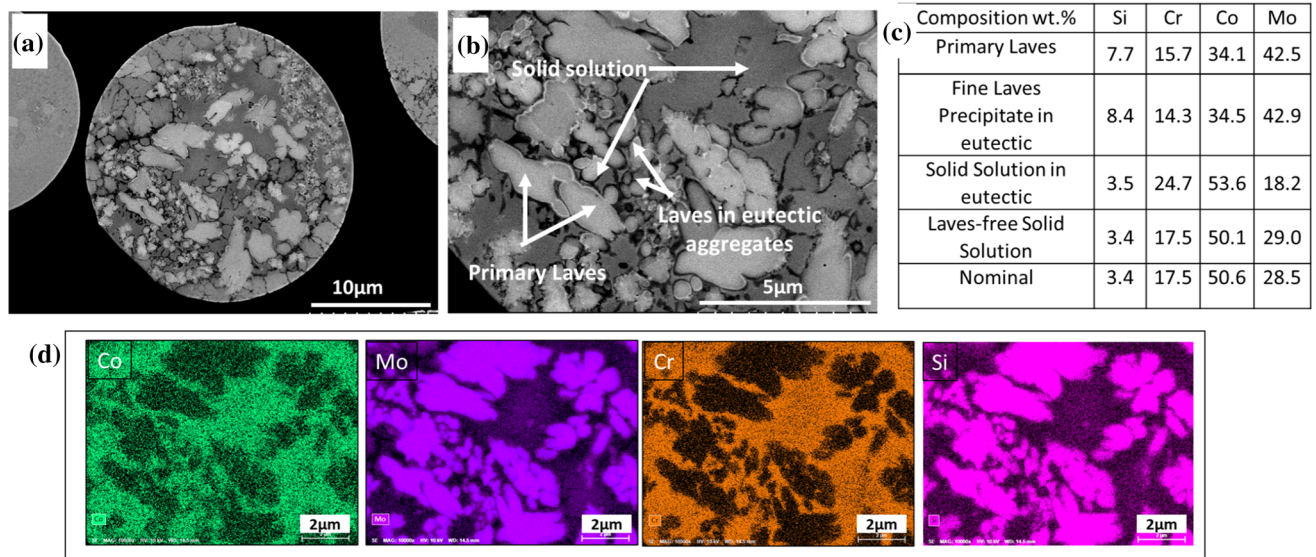


Figure 4 a ECC image of Diamalloy 3001 powders, b high magnification view of (a), c EDS point analysis of various microstructural features, d EDS maps of Co, Mo, Cr, and Si taken in the same region of (b).

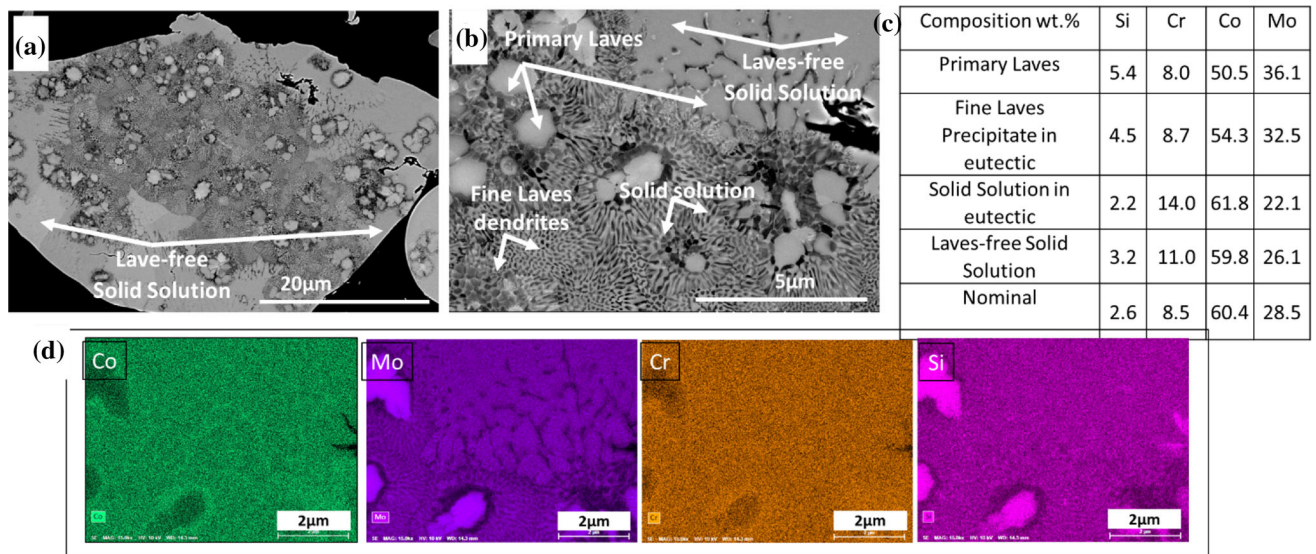


Figure 5 a ECC image of Diamalloy 3002NS powder, b high magnification view of (a), (c) EDS point analysis of various microstructural features, d EDS maps of Co, Mo, Cr, and Si taken in the same region of (b).

leads to the formation of supersaturated solid solutions with a submicron microstructure that were free from Laves phases [10]. In fact, for both Diamalloys, these regions are major constituents among microstructural features. The Laves-free solid solution regions were found to be nano-crystalline with grain size less than 20 nm (Figs. 6d and 7d).

EDS element maps of Laves-containing splats for both Diamalloy coatings are given in Figs. 8 and 9. Point analysis on different microstructural features

was carried out, and the result is given in elemental composition tables. Similar to elemental analysis carried out for powders, the Laves phases either primary or in eutectic aggregates are rich in Mo and Si, whereas they contain lower Co and Cr content as compared to the nominal composition of the alloys. EDS maps were used to visualize the distribution of the constituent elements in the selected regions in coatings. A higher concentration of Co and Cr was identified in solid solutions than Lave phases,

Figure 6 **a** and **b** ECC Images of Diamalloy 3001. **c** and **d** High magnification images of Laves region and Laves-free solid solution, respectively.

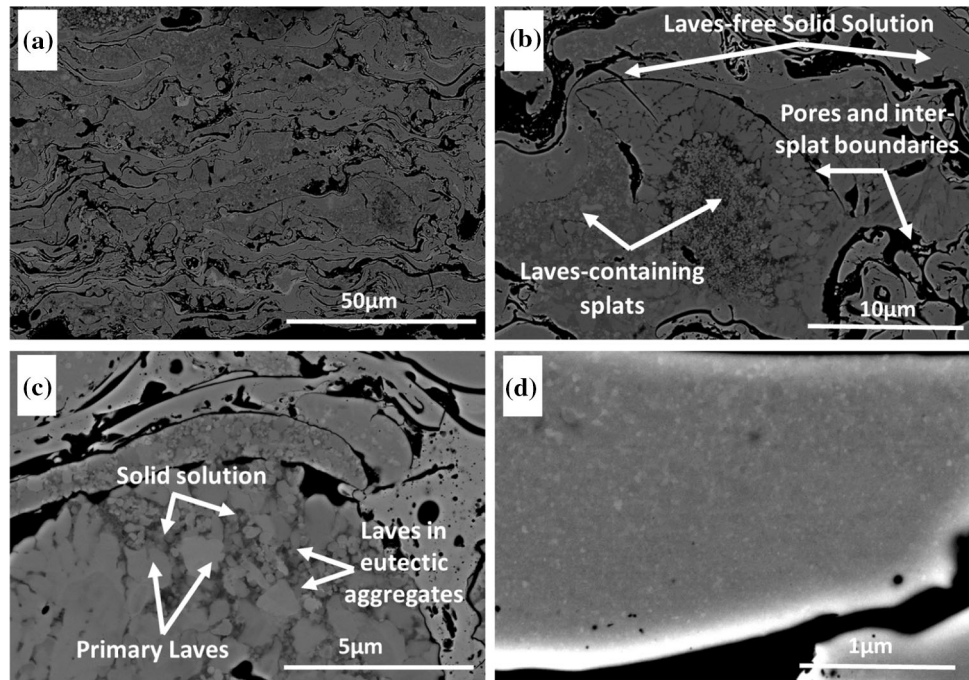


Figure 7 **a** and **b** ECC Images of Diamalloy 3002NS. **c** and **d** High magnification images of Laves region and Laves-free solid solution, respectively.

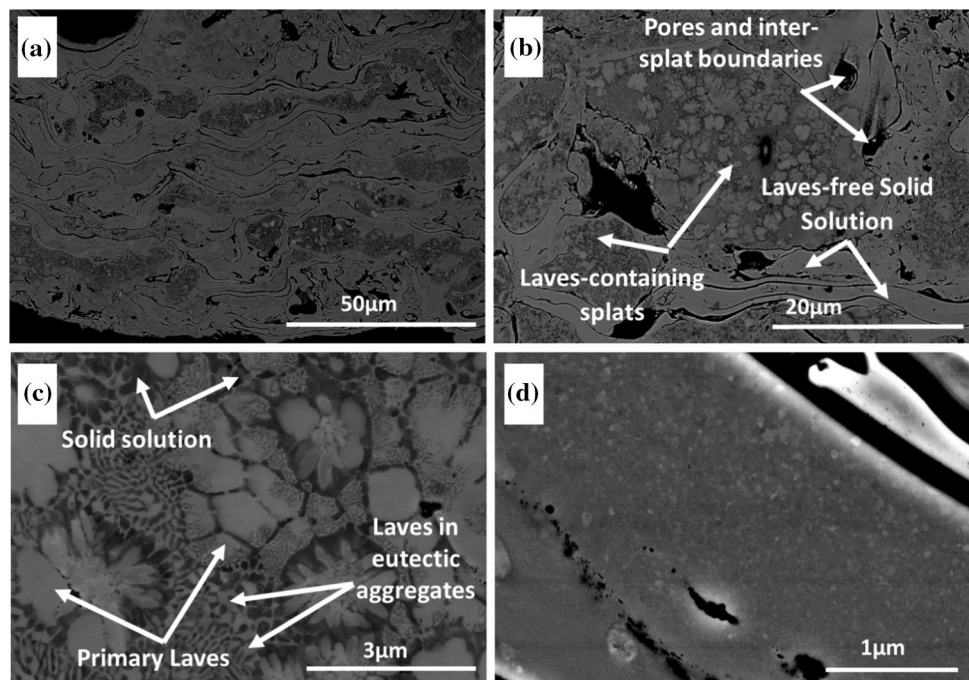


Table 3 Diamalloy 3001 and Diamalloy 3002NS coatings characteristics

Sample designation	Thickness (μm)	Porosity (%)	Primary Laves and eutectic (%)	Laves-free solid solution (%)
Diamalloy 3001	98 ± 6	5 ± 1	36 ± 4	Balance
Diamalloy 3002NS	86 ± 7	3 ± 1	28 ± 4	Balance

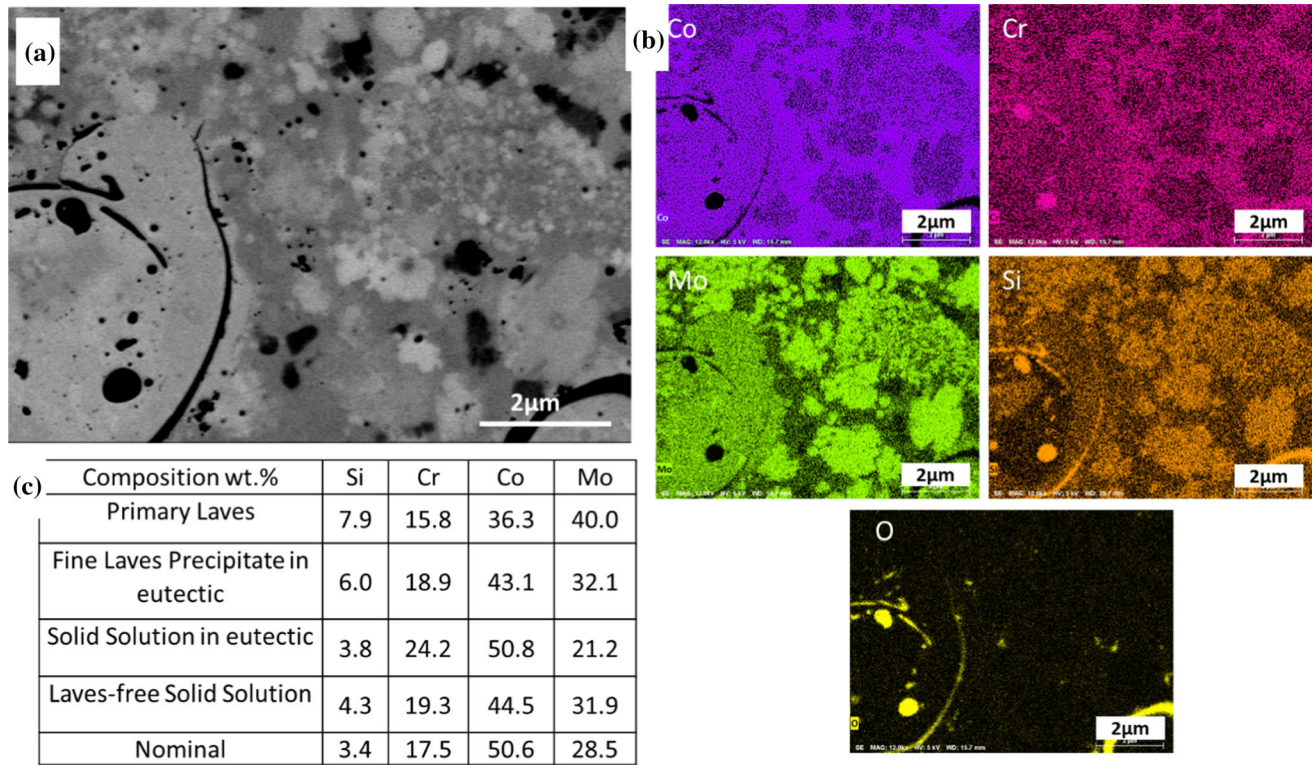


Figure 8 a Backscattered electron (BSE) image of Diamalloy 3001, b EDS maps of Co, Cr, Mo, Si, and O, c EDS composition analysis of solid solution and Laves phases.

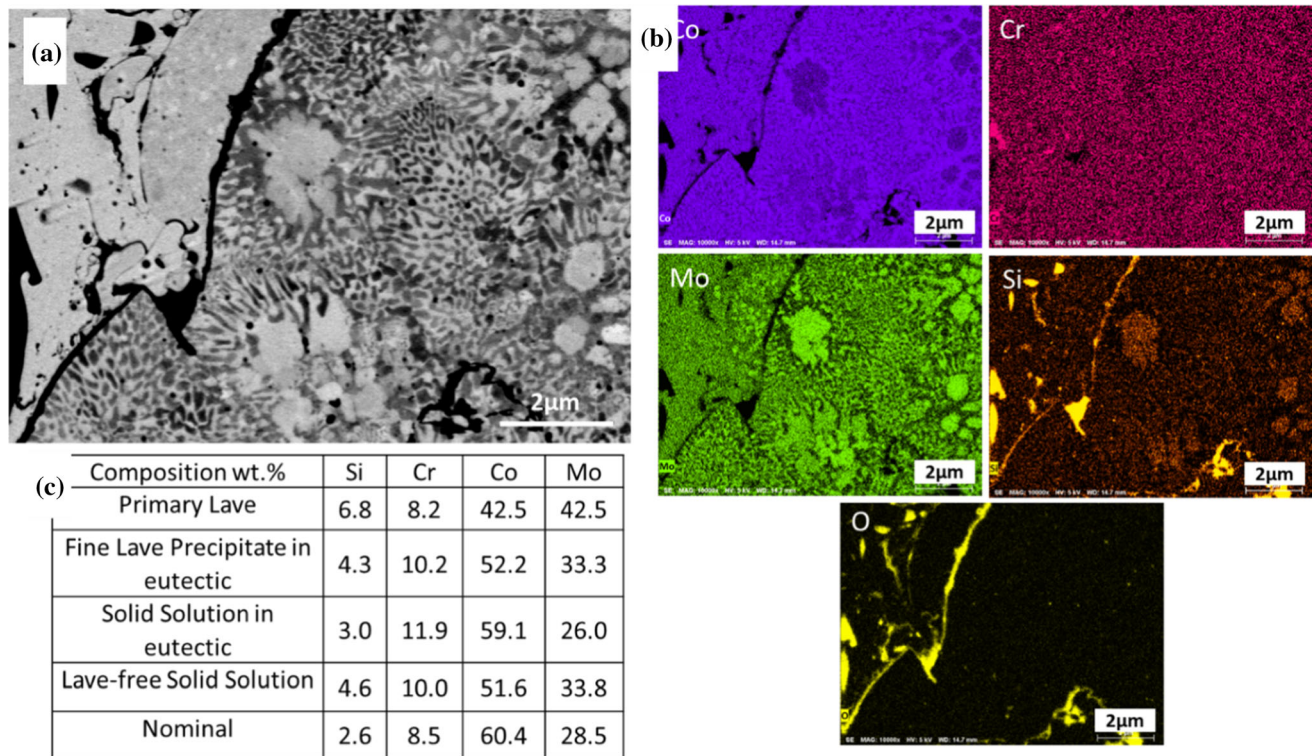


Figure 9 a Backscattered electron (BSE) image of Diamalloy 3001, b EDS maps of Co, Cr, Mo, Si, and O, c EDS composition analysis of solid solution and Laves phases.

whereas for Mo and Si, they were more concentrated in Lave phases as compared to solid solutions. The concentration of Mo and Si was faint for solid solution in maps because they were low in those regions as compared to Lave phases. There were inter-splats gaps in some regions of splat boundaries which is also confirmed by secondary electron (SE) imaging mode. Some regions of splat boundaries gaps contained colloidal silica (SiO_2) which was used for final polishing step in sample preparations. A high concentration of Si and O was obtained in EDS mapping in splat boundaries due to the presence of SiO_2 .

Phase analysis

XRD phase analysis has been performed on the polished top surface of as-sprayed coatings (Fig. 10), and similar phases were indexed to those for powder samples. The main difference, however, is the peaks for $\text{Co}_3\text{Mo}_2\text{Si}$ Laves phase which are now evident on the diffractogram for both materials, indicating this phase is being formed during the spray. The diffraction peaks for spray powders were sharp, while as-sprayed coatings display broad diffraction peaks at $46^\circ < 2\theta < 60^\circ$, which indicates the presence of amorphous or nano-crystalline phases in the as-sprayed coatings. This was also confirmed in ECC images (see Figs. 6 and 7). Previous studies have also reported amorphous or nano-crystalline phases formation in HVOF Triballoys [10] due to the melting and rapid solidification of the material during the spraying process.

An example of the regions that are tested by EBSD, to analyze the phase distribution in Diamalloy 3001 and 3002NS coatings, is given in Fig. 11. Figure 11a shows the BSE image with the insert displaying the region that is tested by EBSD. Band contrast image and phase map images are shown in Fig. 11b–c. Band contrast image (see Fig. 11b) represents the pattern quality. Dark pixels display poor pattern quality, whereas brighter band contrast pixels are of good pattern quality [22]. In Fig. 11b, the Laves-free solid solution regions have poor pattern quality. This is due to a nano-crystalline microstructure identified in these regions, where the lateral resolution defined by the step size (250 nm) was larger than the microstructural scale. For the Laves-containing region, based on XRD phase analysis and previous studies, six intermetallic $\text{Co}_3\text{Mo}_2\text{Si}$, Co_7Mo_6 , Co_3Mo , CoSi_2 , and CoMoSi were selected to index the EBSD

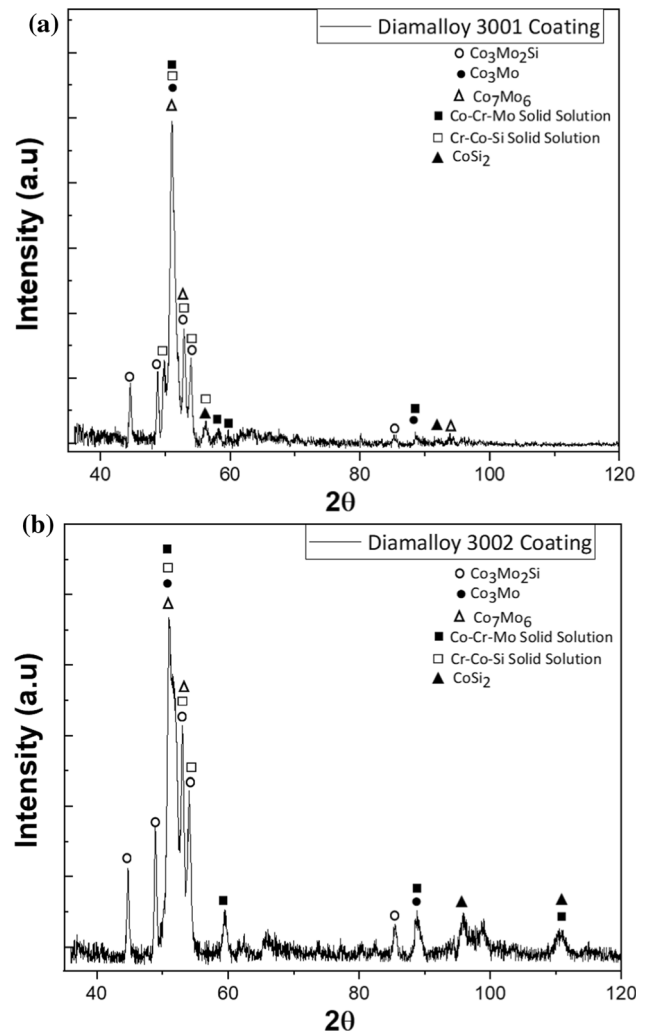


Figure 10 XRD phase characterization of **a** Diamalloy 3001 and **b** Diamalloy 3002NS coatings.

pattern to acquire the phase map (Fig. 11c). The legend displays the corresponding phase color in the phase map. As described in the experimental section, maximum values of 1° for MAD were considered to qualify the solution. Among the six phases mentioned above, $\text{Co}_3\text{Mo}_2\text{Si}$, Co_3Mo , CoSi_2 were found to have acceptable MAD. This is consistent with XRD findings (see Fig. 10). Table 4 summarizes the fraction of these phases identified in coatings. A higher percentage of $\text{Co}_3\text{Mo}_2\text{Si}$ and Co_3Mo was identified on average from the tested regions for both coatings, compared to the CoSi_2 .

Nano- and micro-hardness

Nano-indentation testing was used to measure the hardness of individual phases. An example of nano-

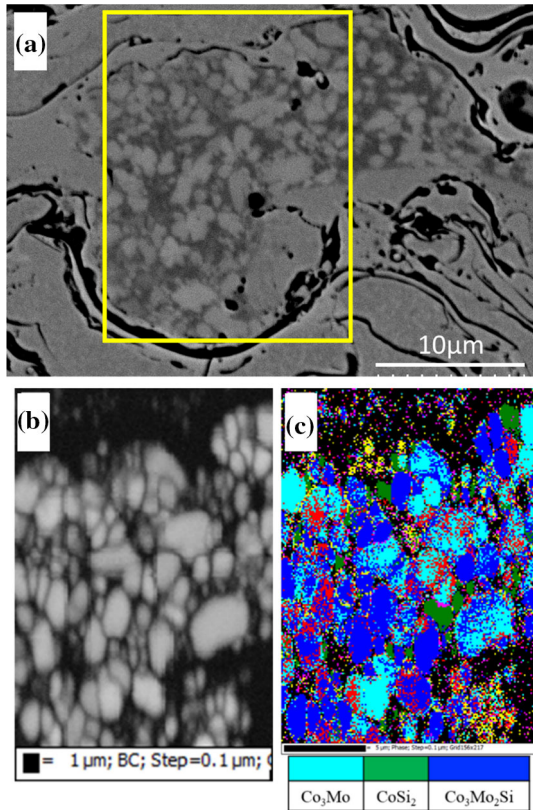


Figure 11 **a** Backscattered electron (BSE) image of Laves region in Diamalloy 3001, **b** band contrast images, **c** phase image with phase legend. **b** and **c** are constructed from EBSD patterns collected from region **(a)**. In **(b)** Dark pixels have poor pattern quality, whereas bright pixels have good pattern quality. In **(c)**, black pixels are non-indexed.

indentation arrays that were performed on the polished cross section of Diamalloy 3001 overlaid with the EBSD phase map is given in Fig. 12. Indents that are located on various phases including Laves-free solid solution as well as Laves phases and solid solution can be seen. Similar hardness values were collected on various phases between two Diamalloy coatings. For both coatings, the Laves-free solid solution (13 ± 1 GPa) was harder than the solid solution in eutectic aggregates (11 ± 1 GPa). $\text{Co}_3\text{Mo}_2\text{Si}$ and Co_3Mo displayed a similar hardness of 13 ± 1 GPa, whereas CoSi_2 was significantly softer (9 ± 2).

Table 4 Diamalloy 3001 and Diamalloy 3002NS coatings

Sample designation	Fraction of phases in Laves regions (%)			Hardness HV _{300gf}
	CoSi ₂	Co ₃ Mo	Co ₃ Mo ₂ Si	
Diamalloy 3001	20 ± 7	40 ± 1	40 ± 8	527 ± 58
Diamalloy 3002NS	11 ± 5	44 ± 5	45 ± 1	571 ± 49

Micro-hardness testing was performed on the polished cross sections of sprayed coating using 300gf load which caused indent imprints of 30 µm on average. This was large enough to include few splats and represent the average hardness of coatings. Diamalloy 3002NS coatings displayed slightly higher hardness compared to Diamalloy 3001 coatings (571 ± 49 vs 527 ± 58 HV_{300gf}), despite having a lower fraction of intermetallic phases (see Table 3 and 4). The properties of phases were similar between the two coatings. However, the concentration of phases was different between the two coatings. The fraction of CoSi_2 , a phase which was shown to have lower hardness among the intermetallic phases being analyzed, was higher for Diamalloy 3001 by a factor of two. Moreover, Diamalloy 3001 coating has higher porosity than Diamalloy 3002NS, which is detrimental to the micro-hardness values.

Spray conditions and particle morphology can affect particle temperature and velocity, changing the amount of melted and partially melted particles while also affecting oxidation. Thus, coating properties can change significantly for different spray conditions reported in previous studies. Bolelli et al. [23] reported a hardness of 6.56 GPa ($\sim 668\text{HV}_{50gf}$) when using a load of 0.5 N for a Diamalloy 3001 sprayed by HVOF. The powder feedstock had the same nominal composition to the Diamalloy 3001 presented in the current study, but it was water atomized, which resulted in a non-spherical powder morphology similar to Diamalloy 3002NS. However, when using a higher load (1 N), Bolelli et al. [10] also reported 7.4 GPa ($\sim 755\text{HV}_{100gf}$) for a gas atomized coating with similar composition of the Diamalloy 3001. Meanwhile, Sahraoui et al. [3] tested a HVOF-sprayed Tribaloy T400, observing a hardness of 703HV when using a load of 300gf at the top surface of the coating. Yang et al. [24] reported the micro-hardness ranging 550–650 HV_{300gf} for CoMoCrSi Co-based coatings (similar to Tribaloy T-800) which were prepared by HVOF under different spraying parameters, with denser coatings (porosity < 0.8%). Cho et al. [25] observed a dependency of the hardness (ranging

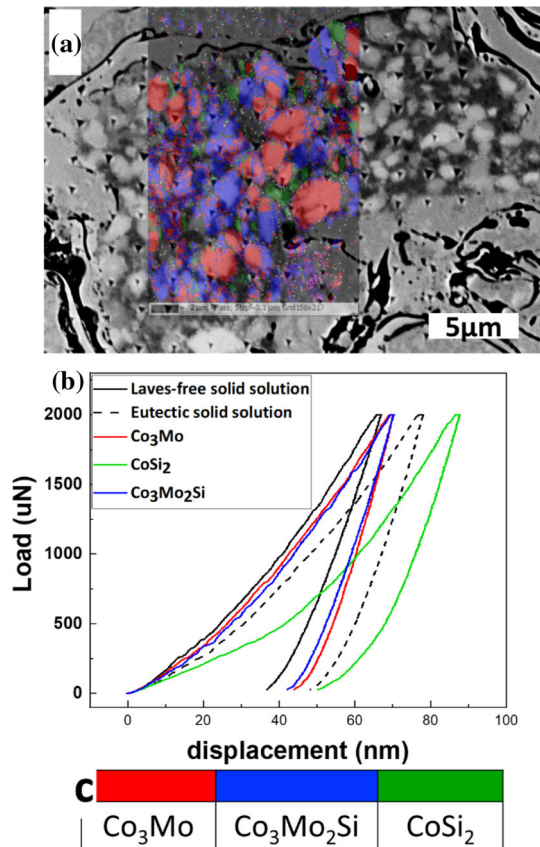


Figure 12 A BSE image of Laves-containing splat in Diamalloy 3001 tested with nano-indentation overlaid with EBSD phase map. Nano-indentation was performed to measure individual phases' hardness. **b** Representative load–displacement curves. **c** Phase legend.

from 560 to a maximum of 638HV_{300gf}) as the spray parameters were modified (either increasing fuel, oxygen or feed rate) leading to various fraction of porosities. The spray conditions used in this study were provided by the manufacturer, which are usually optimized for productivity and not necessarily for mechanical properties which might explain why these coatings are inside the lower range of data reported in the literature.

Scratch adhesion

Scratch adhesion testing was performed on cross section of coatings. Two types of failure can generally be identified during cross-sectional scratch testing: Adhesive failure occurs when failure originates at the interface between the substrate and sprayed coating. If failure originates within the coating, then failure is deemed cohesive. No adhesive failure was observed

in the results obtained for this discussion. A cohesive failure occurred within the coating in the form of a cone extracted by the indenter; therefore, scratch testing allowed characterization of coating cohesion, and the analyzed failure mechanisms are purely cohesive. Analysis of this cone and its projected area allows the cohesive strength of thermal spray coatings to be evaluated. Indeed, a higher projected cone area indicates a lower cohesive strength of the sample [26].

The projected area of the cone extracted by the indenter (cohesive damage) during a scratch test has a monotonic relationship with the applied normal load of the scratch [27]. Figure 13 shows the projected cone area recorded after scratch testing of Diamalloy 3001 and Diamalloy 3002NS plotted against the applied normal scratch load. It can be observed visually that the relationship between projected cone area and applied load is nearly identical for both coating systems. Furthermore, at all tested normal loads, the projected cone area mean averages recorded for both coating systems were statistically similar according to a Student *T* test. This indicates that Diamalloy 3001 and Diamalloy 3002NS coating systems exhibit the same cohesive strengths at loads up to 5 N under identical scratch testing conditions.

The nearly linear relationship between the projected cone area and applied normal load observed in Fig. 13 for both coating systems implied the existence of only one cohesive failure mechanism for the analyzed loading range. Figure 14 shows SEM images of the cohesive damage cone formed by a 3 N normal

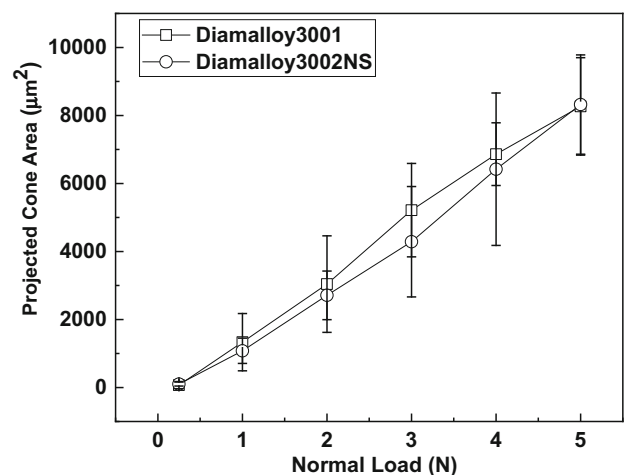
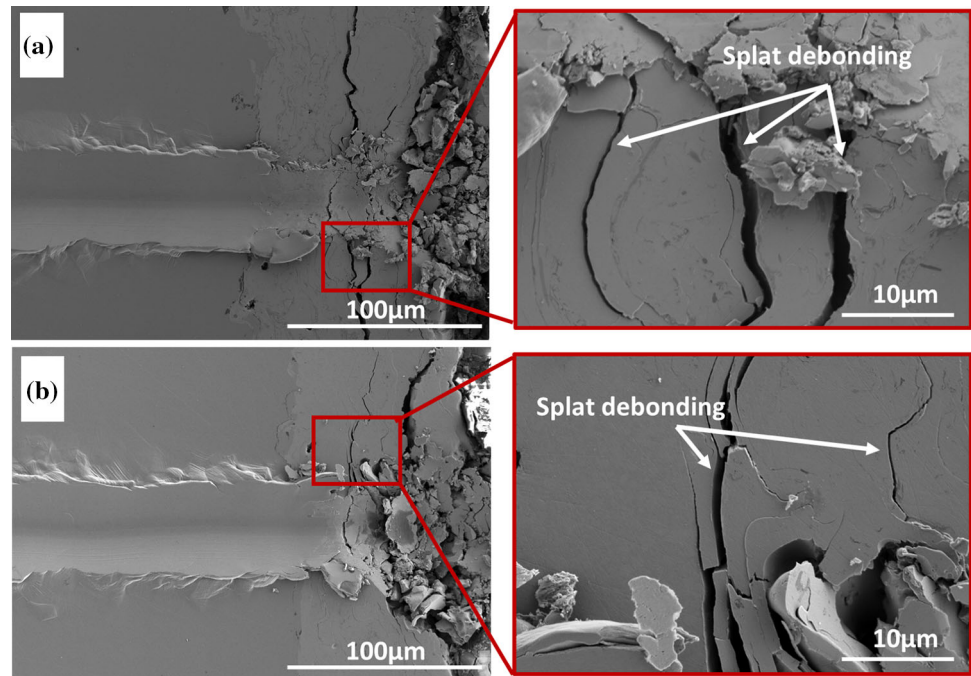


Figure 13 Projected cone area vs normal scratch load for Diamalloy 3001 and Diamalloy 3002NS coatings.

Figure 14 SEM Images of splat debonding cohesive failures in **a** Diamalloy 3001 and **b** Diamalloy 3002NS under 3 N normal force scratch cones.



load scratch for Diamalloy 3001 and Diamalloy 3002NS. Splat debonding was observed in both coatings at all loading conditions, with highly flattened splats providing easy paths for crack propagation. Highly flattened splats underwent melting and solidification, upon which shrinking of the splat occurs. This can lead to debonding to accommodate the thermal stresses from the shrinking of the splat. Therefore, highly flattened particles act like weak inter-splat boundaries and fail earlier when subjected to scratch testing. The cohesive failure mechanism for both coating systems under the examined conditions can therefore be identified as splat debonding. As the only present failure mechanism, it can be stated that Diamalloy 3001 and Diamalloy 3002NS coatings have similar inter-splat bond strengths despite their differences in composition, porosity, and phase distribution.

Conclusion

Two CoMoCrSi Diamalloy 3001 and 3002NS coatings were deposited on mild steel using HVOF. Supersaturated Laves-free solid solution, primary Laves phase as well as eutectic aggregate were found to be present for both coatings. Highly flattened splats consisted of supersaturated solid solution and possess nano-crystalline structure. HVOF Diamalloy

coatings had lower fraction of Laves phases, compared to similar coatings processed by laser cladding or casting. This was due to very high cooling rate upon HVOF deposition, where there was not enough time for Laves phases to develop. Although, HVOF Diamalloy coatings had lower percentage of Laves phases, it was found that non-equilibrium supersaturated structure was useful in strengthening the alloy as they displayed similar nano-hardness values to those of Laves phases. However, the properties of non-equilibrium supersaturated phases can be altered when service conditions cause re-crystallization and grain growth. Weak inter-splat bonding between highly flattened splats led to splat debonding in scratch cohesion testing. The two coatings displayed similar qualitative splat cohesion strength. Diamalloy 3002NS coatings displayed slightly higher hardness compared to Diamalloy 3001 coatings, despite having lower percentage of primary Laves phases.

References

- [1] Wielage B, Wank A, Pokhmurska H, Grund T, Rupprecht C, Reisel G, Friesen E (2006) Development and trends in HVOF spraying technology. *Surf Coat Technol* 201:2032–2037

- [2] Schmidt RD, Ferriss DP (1975) New materials resistant to wear and corrosion to 1000°C. *Wear* 32:279–289
- [3] Sahraoui T, Fenineche NE, Montavon G, Coddet C (2004) Alternative to chromium: characteristics and wear behavior of HVOF coatings for gas turbine shafts repair (heavy-duty). *J Mater Process Technol* 152:43–55
- [4] Sahraoui T, Faraoun HI, Fenineche NE, Montavon G, Aourag H, Coddet C (2004) HVOF-sprayed Tribaloy®-400: microstructure and first principle calculations. *Mater Lett* 58:2433–2436
- [5] Navas C, Cadenas M, Cuetos JM, de Damborenea J (2006) Microstructure and sliding wear behaviour of Tribaloy T-800 coatings deposited by laser cladding. *Wear* 260(7):838–846
- [6] Tobar MJ, Amado JM, Álvarez C, García A, Varela A, Yáñez A (2008) Characteristics of Tribaloy T-800 and T-900 coatings on steel substrates by laser cladding. *Surf Coat Technol* 202(11):2297–2301
- [7] Przybylowicz J, Kusinski J (2000) Laser cladding and erosive wear of Co–Mo–Cr–Si coatings. *Surf Coat Technol* 125(1):13–18
- [8] Díaz E, Amado JM, Montero J, Tobar MJ, Yáñez A (2012) Comparative study of Co-based alloys in repairing low Cr–Mo steel components by laser cladding. *Phys Proc* 39:368–375
- [9] Ya W, Pathiraj B, Matthews DTA, Bright M, Melzer S (2018) Cladding of Tribaloy T400 on steel substrates using a high power Nd:YAG laser. *Surf Coat Technol* 350:323–333
- [10] Bolelli G, Cannillo V, Lusvardi L, Montorsi M, Mantini FP, Barletta M (2007) Microstructural and tribological comparison of HVOF-sprayed and post-treated M–Mo–Cr–Si (M=Co, Ni) alloy coatings. *Wear* 263(7):1397–1416
- [11] Singh S, Guo Y, Winiarski B, Burnett TL, Withers PJ, De Graef M (2018) High resolution low kV EBSD of heavily deformed and nanocrystalline Aluminium by dictionary-based indexing. *Sci Rep* 8(1):10991
- [12] Edwards TEJ, Di Gioacchino F, Muñoz-Moreno R, Clegg WJ (2017) The interaction of borides and longitudinal twinning in polycrystalline TiAl alloys. *Acta Mater* 140:305–316
- [13] Zhu C, Kaufmann K, Vecchio KS (2020) Novel remapping approach for HR-EBSD based on demons registration. *Ultramicroscopy* 208:112851
- [14] Oliver WC, Pharr GM (1992) An improved technique for determining hardness and elastic-modulus using load and displacement sensing indentation experiments. *J Mater Res* 7(6):1564–1583
- [15] Fischer-Cripps AC (2002) *Nanoindentation*. Springer, Mechanical engineering series
- [16] Hysitron TI 950 Triboindenter User Manual Revision 9.3.0314 Hysitron Incorporated 2014.
- [17] Vencl A, Arostegui S, Favaro G, Zivic F, Mrdak M, Mitrović S, Popovic V (2011) Evaluation of adhesion/cohesion bond strength of the thick plasma spray coatings by scratch testing on coatings cross-sections. *Tribol Int* 44(11):1281–1288
- [18] ISO27307:2015, Thermal spraying—Evaluation of adhesion/cohesion of thermal sprayed ceramic coatings by transverse scratch testing. Geneva, Switzerland, 2015.
- [19] Boulnat X, Lafont C, Coudert JB, Dayot C (2020) Microstructure evolution of fine-grained cobalt T400 Tribaloy processed by Spark Plasma Sintering or Hot Isostatic pressing of gas-atomized powders. *Metall and Mater Trans A* 51(10):5318–5327
- [20] Halstead A, Rawlings RD (1984) Structure and hardness of Co–Mo–Cr–Si wear resistant alloys (Triballoys). *Metal Sci* 18(10):491–500
- [21] Mason SE, Rawlings RD (1994) Effect of iron additions on microstructure and mechanical properties of Ni–Cr–Mo–Si hardfacing alloy. *Mater Sci Technol* 10(10):924–928
- [22] Prior DJ, Wheeler J, Peruzzo L, Spiess R, Storey C (2002) Some garnet microstructures: an illustration of the potential of orientation maps and misorientation analysis in microstructural studies. *J Struct Geol* 24(6):999–1011
- [23] Bolelli G, Cannillo V, Lusvardi L, Riccò S (2006) Mechanical and tribological properties of electrolytic hard chrome and HVOF-sprayed coatings. *Surf Coat Technol* 200(9):2995–3009
- [24] Yang W-J, Zou L, Cao X-Y, Liu J-H, Li D-J, Cai Z-B (2019) Fretting wear properties of HVOF-sprayed CoMoCrSi coatings with different spraying parameters. *Surf Coat Technol* 358:994–1005
- [25] Cho JY, Zhang SH, Cho TY, Yoon JH, Joo YK, Hur SK (2009) The processing optimization and property evaluations of HVOF Co-base alloy T800 coating. *J Mater Sci* 44(23):6348–6355
- [26] Bull SJ (1999) Can scratch testing be used as a model for the abrasive wear of hard coatings. *Wear* 233:412–423
- [27] Vencl A, Gligorijevi B, Katavi B, Nedi B, Eüni D (2013) In: Abrasive wear resistance of the iron- and WC-based hardfaced coatings evaluated with scratch test method, 2013.

Publisher's Note Springer Nature remains neutral with regard to jurisdictional claims in published maps and institutional affiliations.

Springer Nature or its licensor (e.g. a society or other partner) holds exclusive rights to this article under a publishing agreement with the author(s) or other rightsholder(s); author self-archiving of the accepted manuscript version of this article is solely governed by the terms of such publishing agreement and applicable law.